12-1-2020

Chandra Spectral Measurements Of The O Supergiant ζ Puppis Indicate A Surprising Increase In The Wind Mass-Loss Rate Over 18 Yr

David H. Cohen
Swarthmore College, dcohen1@swarthmore.edu

Jiaming Wang , '22

V. Petit

M. A. Leutenegger

L. Dakir

See next page for additional authors

Follow this and additional works at: https://works.swarthmore.edu/fac-physics

Part of the Astrophysics and Astronomy Commons

Let us know how access to these works benefits you

Authors

David H. Cohen; Jiaming Wang , '22; V. Petit; M. A. Leutenegger; L. Dakir; C. Mayhue , '23; and A. David-Uraz

Chandra spectral measurements of the O supergiant ζ Puppis indicate a surprising increase in the wind mass-loss rate over 18 yr

David H. Cohen [⊙],[1][★] Jiaming Wang,[1] Véronique Petit [⊙],[2] Maurice A. Leutenegger [⊙],[3] Lamiaa Dakir,[4] Chloe Mayhue[1] and Alexandre David-Uraz [⊙][2]

[1]*Department of Physics and Astronomy, Swarthmore College, Swarthmore, PA 19081, USA*
[2]*Department of Physics and Astronomy & Bartol Research Institute, University of Delaware, Newark, DE 19716, USA*
[3]*NASA/Goddard Space Flight Center, Code 662, Greenbelt, MD 20771, USA*
[4]*Bryn Mawr College, Bryn Mawr, PA 19010, USA*

ABSTRACT

New long *Chandra* grating observations of the O supergiant ζ Pup show not only a brightening of the X-ray emission line flux of 13 per cent in the 18 yr since *Chandra*'s first observing cycle, but also clear evidence – at more than 4σ significance – of increased wind absorption signatures in its Doppler-broadened line profiles. We demonstrate this with non-parametric analysis of the profiles as well as Gaussian fitting and then use line-profile model fitting to derive a mass-loss rate of $2.47 \pm 0.09 \times 10^{-6}$ $M_{\odot}$ yr^{-1}, which is a 40 per cent increase over the value obtained from the cycle 1 data. The increase in the individual emission line fluxes is greater for short-wavelength lines than long-wavelength lines, as would be expected if a uniform increase in line emission is accompanied by an increase in the wavelength-dependent absorption by the cold wind in which the shock-heated plasma is embedded.

Key words: radiative transfer – stars: early-type – stars individual: ζ Puppis – stars: massive – stars: mass-loss – stars: winds, outflows – X-rays: stars.

1 INTRODUCTION

Resolved X-ray emission line profiles provide diagnostic information about both the X-ray production in the dense, highly supersonic radiation-driven winds of O stars, and also about the mass-loss rates of these winds. Indeed, one of the first results for massive stars provided by the *Chandra* spectrometers soon after the observatory's launch in 1999 was the confirmation that these X-rays arise in the stellar wind, rather than in a magnetically confined corona, as is the case for low-mass stars. This was revealed by the very significant Doppler broadening (half width at half-maximum ≈ 1000 km s^{-1}) in the X-ray emission line profiles of the canonical single O supergiant, ζ Pup (Kahn et al. 2001; Cassinelli et al. 2001).

In addition to verifying the wind origin of the X-rays in O stars, measuring resolved X-ray line profiles enables us to constrain the spatial distribution of the wind-shocked plasma, as there is a mapping between distance from the photosphere and wind speed. Analysis of the cycle 1 *Chandra* grating spectra of ζ Pup (taken in 2000) showed that the X-ray emission begins about half a stellar radius into the wind flow, as expected for embedded wind shocks (EWS) produced by the line-deshadowing instability (Cohen et al. 2010), and this result holds for other O stars with strong winds observed by *Chandra* (Cohen et al. 2014).

The line profiles are also affected by continuum absorption in the cold component of the wind, primarily from K-shell photoionization of metals. This attenuation preferentially affects the rear, red-shifted hemisphere of the wind, leading to characteristically blue-shifted and asymmetric profiles, with the degree of asymmetry being governed by the wind column density and hence, mass-loss rate (MacFarlane et al. 1991; Ignace 2001; Owocki & Cohen 2001). Owocki & Cohen (2001) presented a line profile model with three free parameters: line flux, X-ray onset radius ($R_{\rm o}$), and characteristic wind optical depth (τ_*), which can be fit to individual resolved X-ray lines. The optical depth parameter, τ_*, is a function of wavelength via the wavelength dependence of bound-free continuum opacity in the cool wind, and so every line in a given spectrum is expected to have an optical depth proportional to the wind opacity at the wavelength of that line, and the ensemble of fitted τ_* values can be used to derive a wind mass-loss rate. This procedure was used to fit 16 lines and line complexes in the cycle 1 *Chandra* spectrum of ζ Pup, and it was found that a single X-ray onset radius of $R_{\rm o} = 1.5\,R_*$ is consistent with the fitting results of all the lines, while the individual line's fitted τ_* values gave a mass-loss rate of $1.76^{+0.13}_{-0.12} \times 10^{-6}$ $M_{\odot}$ yr^{-1} (Cohen et al. 2014).

X-ray emission from EWS in O stars is generally not variable on short time-scales comparable to wind flow and shock cooling times (hours), which is taken as an indication that a very large number of wind shock zones contribute to the overall X-ray emission (Nazé, Oskinova & Gosset 2013). Wind properties of O stars, including ζ Pup, often show cyclical short-term variability (Howarth, Prinja & Massa 1995; Massa et al. 1995), but the global wind properties –

Table 1. *Chandra* Observing Log.

Observation ID	Exposure time (ks)	Date	Cycle number
640	67.74	2000 Mar 28	1
21113	17.72	2018 Jul 1	19
21112	29.70	2018 Jul 2	19
20156	15.51	2018 Jul 3	19
21114	19.69	2018 Jul 5	19
21111	26.86	2018 Jul 6	19
21115	18.09	2018 Jul 7	19
21116	43.39	2018 Jul 8	19
20158	18.41	2018 Jul 30	19
21661	96.88	2018 Aug 3	19
20157	76.43	2018 Aug 8	19
21659	86.35	2018 Aug 22	19
21673	14.95	2018 Aug 24	19
20154	46.97	2019 Jan 25	19
22049	27.69	2019 Feb 1	19
20155	19.69	2019 Jul 15	19
22278	30.51	2019 Jul 16	19
22279	26.05	2019 Jul 17	19
22280	25.53	2019 Jul 20	19
22281	41.74	2019 Jul 21	19
22076	75.12	2019 Aug 1	19
21898	55.70	2019 Aug 17	19

including the mass-loss rate – seem to be quite constant in normal O stars. However, a long X-ray observing campaign with *XMM* showed that the overall X-ray emission levels of ζ Pup are variable with an amplitude of variability of about 20 per cent, but no clear time-scale of variability,[1] though longer than ∼10^5 s (Nazé et al. 2013).

During cycle 19, *Chandra* carried out a long sequence of 21 observations of ζ Puppis with the High Energy Transmission Grating Spectrometer (HETGS). In this paper, we present results from the analysis of the ten measurable lines and line complexes in these data and compare them to those previously obtained from the cycle 1 data set, taken 18 yr earlier, specifically focusing on the wind optical depths and mass-loss rate.

In Section 2 we describe the data, its reduction, and the three different approaches we use for analysing the line profile shapes. In Section 3, we present the results of the line profile fitting. In Section 4, we discuss the modelling results, including changes in the X-ray and wind properties between the two sets of observations, which imply a large change in the mass-loss rate, and in Section 5 we summarize our conclusions.

2 DATA, ANALYSIS, AND MODELLING

Nearly 813 ks of new *Chandra* observations (PI: W. Waldron) were obtained during cycle 19, between 2018 July and 2019 August, in 21 separate pointings (designated by a unique *Observation ID*, or Obs ID) ranging in exposure time from just over 10 ks to almost 100 ks. We present an observing log in Table 1, which also includes the lone Obs ID from cycle 1, taken 18 yr earlier.

The *Chandra* HETGS contains two grating arrays – the medium energy grating (MEG) and high-energy grating (HEG) (Canizares et al. 2005). We reprocessed the data retrieved from the archive in

---

[1]Due to the relatively large wavelength calibration uncertainties of the *XMM* reflection grating spectrometer, it is not possible to ascertain whether the line profiles vary from observation to observation.

2019 November using the CIAO pipeline (v. 4.11), including CALDB (v. 4.8.5), producing response matrix files and auxiliary response files (containing effective area information), along with extracted first-order spectra for both the MEG and HEG. We do not subtract a background when we analyse the data.

We show the MEG and HEG spectra for all the cycle 19 observations, combined, in Fig. 1. Note that this is for illustration only. Inspecting the combined 21 Obs IDs, we identify seven individual lines and three He-like line complexes that can be analysed. Due to the deterioration of the long-wavelength sensitivity there are several lines (and line complexes) seen in the cycle 1 data that we do not detect in the cycle 19 data, even when all Obs IDs are combined.

All the line analysis we present here is performed on the 21 separate data sets, with each data set consisting of a co-added (±1 order) MEG spectrum and a co-added (±1 order) HEG spectrum. For each line or line complex we analyse, we treat these 42 spectra as a single data set. We do not combine them, rather we analyse them simultaneously. We use XSPEC v. 12.9 to fit a flat spectral model to carefully selected continuum regions on either side of each of the lines and line complexes. We use this continuum modelling for all of the analyses presented in this section, and in Appendix A we provide details, including figures, describing the continuum fits.

Prior to fitting the wind-profile model from which wind optical depths and the wind mass-loss rate can be measured, we analyse the seven single lines in the spectra in two model-independent ways: (1) a moment analysis that treats each line profile as a probability distribution (Cohen et al. 2006) and (2) fitting Gaussian profiles.

For the moment analysis, we co-add the 21 Obs IDs, subtract the continuum model from the line, convert the wavelength scale to a unitless Doppler shift scaled to the wind terminal velocity, $x \equiv (\frac{\lambda}{\lambda_0} - 1)\frac{c}{v_\infty}$, and compute the first moment – the centroid shift of each line according to

$$M_1 \equiv \frac{\Sigma_{i=1}^N x_i f(x_i)}{\Sigma_{i=1}^N f(x_i)},$$

where f is the count rate in each bin and sums are over the N data points on $x = [-1:1]$. We do this for each of the seven individual lines (not the heavily blended He-like complexes), analysing the MEG and HEG data separately, and present the weighted average of the MEG and HEG results for each line in Table 2 and Fig. 2.

For the Gaussian fitting, we fit a Gaussian line profile model on top of a power-law continuum model, with the continuum model's flux level fixed (at the same level used for the moment analysis and the wind profile fitting). We allow the normalization, centroid, and width of the Gaussian to be free parameters and show the results for the centroid and width, both in km s^{-1}, in Table 2 and Fig. 3.

Both the first moment and the Gaussian centroid become more negative between cycle 1 and cycle 19 for six of the seven lines, indicating that the emission lines are systematically more blue-shifted, as would be expected from an increase in wind absorption. In the aggregate, this result – that the first moment has increased – is significant at the 3σ level. The Gaussian widths also increase significantly between cycles 1 and 19, which is an expected effect of the line profile shape change associated with increased wind absorption (Owocki & Cohen 2001).

Given these indications of morphological changes in the profile shapes consistent with the wind optical depths increasing, we next fit the wind profile model that has been used to derive mass-loss rates for O stars from *Chandra* grating spectra. The characteristic optical
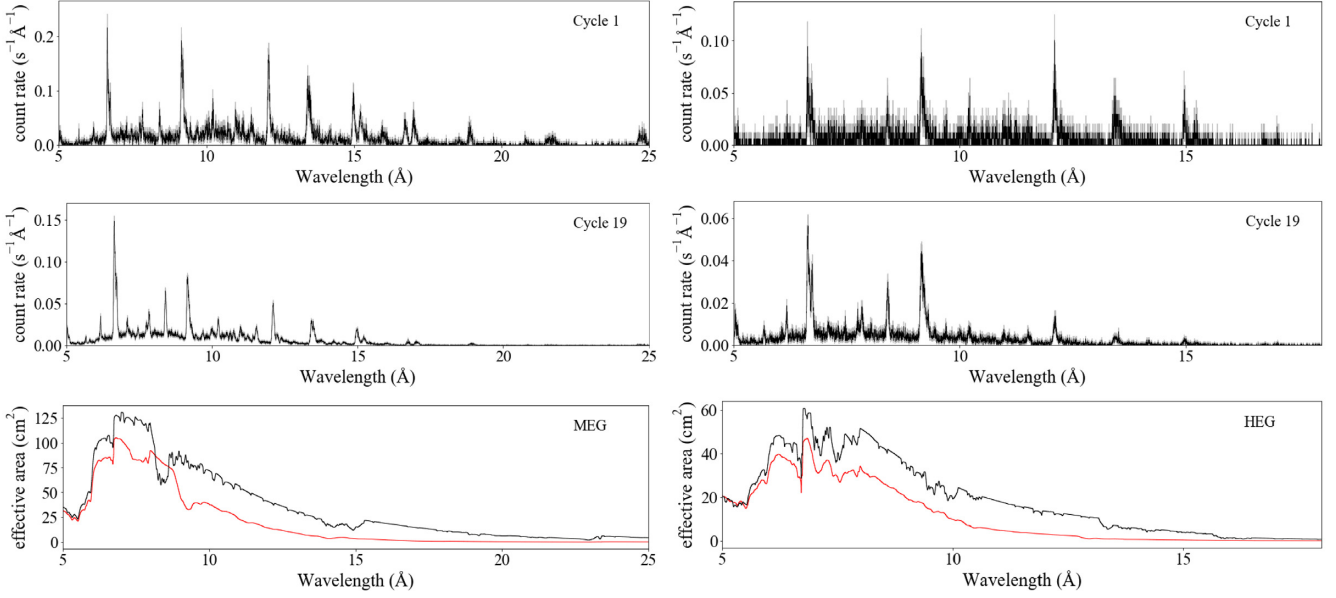
Figure 1. The first-order co-added ±1 MEG (left) and HEG (right) spectra for cycle 1 and the combined cycle 19 observations are shown in the first two rows. The last row shows the exposure-time-weighted average effective area of the *Chandra* MEG (left) and HEG (right) at the time of each observation, with the cycle 1 effective in black and the cycle 19 effective area in red. Although count rates are generally lower in the cycle 19 data, modelling we present in Section 3 shows that the X-ray flux of ζ Pup has actually increased between cycle 1 and cycle 19.

Table 2. Line profile moment and Gaussian fit results of emission line profiles for cycle 1 and cycle 19.

| Ion	Wavelength (Å)	M_1 (cycle 1)	M_1 (cycle 19)	Centroid shift (cycle 1, km s^{-1})	Centroid shift (cycle 19, km s^{-1})	Width (cycle 1, km s^{-1})	Width (cycle 19, km s^{-1})
Si XIV	6.18	-0.074 ± 0.077	-0.151 ± 0.022	-281^{+161}_{-170}	-330^{+35}_{-36}	827^{+217}_{-202}	636^{+36}_{-35}
Mg XII	8.42	-0.114 ± 0.038	-0.165 ± 0.010	-421^{+73}_{-71}	-414^{+20}_{-20}	697^{+85}_{-73}	760^{+19}_{-18}
Ne X	10.24	-0.184 ± 0.049	-0.242 ± 0.021	-579^{+70}_{-71}	-643^{+35}_{-35}	631^{+69}_{-61}	762^{+37}_{-35}
Ne IX	11.54	-0.096 ± 0.040	-0.197 ± 0.017	-353^{+151}_{-121}	-522^{+38}_{-39}	1121^{+151}_{-121}	880^{+40}_{-37}
Ne X	12.13	-0.287 ± 0.017	-0.313 ± 0.010	-605^{+31}_{-30}	-643^{+19}_{-19}	695^{+30}_{-27}	783^{+18}_{-18}
Fe XVII	15.01	-0.163 ± 0.019	-0.197 ± 0.012	-455^{+40}_{-39}	-474^{+28}_{-27}	820^{+36}_{-33}	951^{+25}_{-24}
Fe XVII	16.78	-0.285 ± 0.036	-0.266 ± 0.032	-678^{+58}_{-58}	-726^{+61}_{-62}	782^{+52}_{-48}	945^{+66}_{-61}
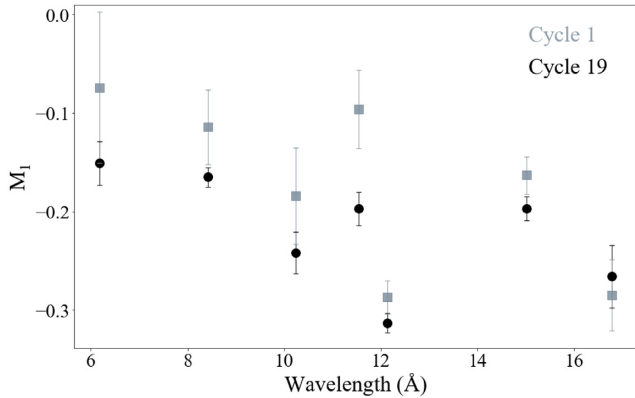
Figure 2. The first moment of each unblended line profile can be seen to change systematically between cycle 1 and cycle 19.

depth parameter

$$\tau_* = \frac{\kappa_\lambda \dot{M}}{4\pi R_* v_\infty}$$

enables the determination of the wind mass-loss rate given a model of the wavelength-dependent wind opacity, κ_λ. We use the same solar metallicity wind opacity model here that was used in Cohen et al. (2014).

We use the *windprof* local model[2] in XSPEC and for the helium-like line complexes in the spectra, we use the variant *hewind* that implements a superposition of three profile models at the appropriate wavelengths and incorporates alteration of the forbidden-to-intercombination line ratio according to the model's assumed spatial distribution of the X-ray-emitting plasma (governed by R_o). We find best-fitting model parameters by minimizing the C statistic, which is necessary for these unbinned data that have many bins with few counts in the line wings (Cash 1979). We then place confidence limits on each of the three model parameters (flux, R_o, τ_*) using the ΔC formalism (Nousek & Shue 1989), one at a time, with the other two parameters free to vary. We use 68 per cent confidence limits ($\Delta C = 1$) for the line fitting results presented here.

---

[2]Local model documentation and code for both *windprof* (Owocki & Cohen 2001) and *hewind* (Leutenegger et al. 2006) are available at https://heasarc.gsfc.nasa.gov/xanadu/xspec/models/windprof.html.
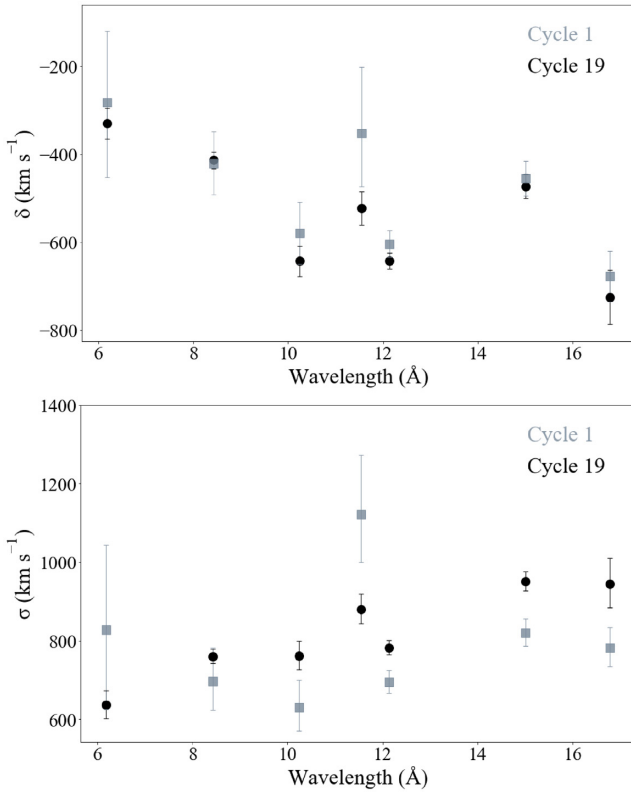
Figure 3. The centroid (top) and width (bottom) of the Gaussian fit to each unblended line profile change systematically between cycle 1 and cycle 19.

3 WIND PROFILE MODEL FITTING RESULTS

The results of fitting each of the 10 lines and line complexes are presented in Table 3. Individual line profile fits are shown in Appendix B.

The optical depth, τ_*, results listed in Table 3 include 68 per cent confidence limits. These confidence limits characterize probability distributions that are sometimes far from Gaussian. We derive a wind mass-loss rate by fitting a model of wavelength-dependent τ_* values to the ensemble of values derived from fitting individual line profiles. Traditionally, this fitting has used χ^2 as a fit statistic and assumed that the uncertainties on that fitted model parameter are Gaussian (Cohen et al. 2014). Here, we relax that assumption and use the actual probability distributions derived from the ΔC values (computed via the *steppar* command in XSPEC) (Cash 1979). We then fit the mass-loss rate to the ensemble of τ_* probability distributions by maximizing the combined probability of the 10 τ_* distributions.

This result is graphically presented in Fig. 4 where we show the τ_* probability distributions and the derived mass-loss rate probability distribution itself, from which we find the best-fitting mass-loss rate and 68 per cent confidence limits of $2.47 \pm 0.09 \times 10^{-6}$ M$_\odot$ yr^{-1}. This mass-loss rate represents a significant increase – more than 4σ – over the value derived from the cycle 1 observations, $\dot{M} = 1.76^{+0.13}_{-0.12} \times 10^{-6}$ M$_\odot$ yr^{-1} (Cohen et al. 2014). We note that we reanalysed the cycle 1 data – including only the same lines analysed in the new cycle 19 data and using this new method, with the fits shown graphically in Appendix B. That reanalysis, shown in Fig. 4, is consistent with the earlier result: $\dot{M} = 1.88^{+0.13}_{-0.14} \times 10^{-6}$ M$_\odot$ yr^{-1}.

The increase in the wind mass-loss rate is accompanied by a corresponding increase in the emission line fluxes between cycle

1 and cycle 19 (already reported by Huenemoerder et al. 2020 for short-wavelength lines), as shown in Fig. 5. This line flux increase averages 13 per cent, but shorter wavelength lines show a consistently larger increase while longer wavelength lines, where the wind opacity is higher, generally show a smaller increase. This is exactly what is expected if all line luminosities increase by the same amount but a corresponding increase in the wind absorption partially compensates for the increase at wavelengths where the wind is optically thick.

4 DISCUSSION

The X-ray luminosity of dense O star winds with radiative shocks is expected to scale linearly with the mass-loss rate (Owocki et al. 2013). So, if the mass-loss rate of ζ Pup has increased by about 40 per cent, the X-ray flux should as well, and that is close to what is seen at short wavelengths where the wind is optically thin (see Fig. 5). The wind is optically thick to longer wavelength line emission and so the emergent flux of longer wavelength lines will not increase the full 40 per cent. This scenario – a 40 per cent increase in wind mass-loss rate between 2000 and 2018 accompanied by roughly the same increase in intrinsic line emission, but because of increased wind absorption, the increase in observed line flux is less than this – is the simplest interpretation of the observed changes to the X-ray properties of ζ Pup.

A mass-loss rate change on years time-scale would indeed be quite surprising for a relatively normal O supergiant like ζ Pup, which is not a luminous blue variable or member of any other class of strongly variable evolved massive stars. It is true that ζ Pup shows small amplitude optical photometric and emission line variability on rotational (days) time-scales that implies photospheric hot spots that drive wind variability (Ramiaramanantsoa et al. 2018). This observed short time-scale periodic variability has a small amplitude and may affect overall mass-loss rates and wind column densities and thus X-ray absorption, but not at the 40 per cent level (David-Uraz et al. 2017; Sundqvist, Owocki & Puls 2018).

The standard line-driven wind theory (Castor, Abbott & Klein 1975) has a scaling of mass-loss rate with bolometric luminosity of roughly $\dot{M} \propto L_{bol}^{1.7}$ (see Owocki & Cohen 1999), suggesting that a brightening of a few tenths of a magnitude may have accompanied a 40 per cent mass-loss rate increase. This is well beyond what is seen in the recent high-cadence photometric monitoring (Ramiaramanantsoa et al. 2018). Perhaps the spot characteristics change on longer time-scales in ways that affect the global mass-loss rate. However, if the global luminosity of the star changes, whether uniformly or via evolving spot characteristics, it would imply a not insignificant internal change to the star. Beating between closely spaced pulsational modes could cause long-time-scale brightness variations, though there is no evidence for this particular behaviour in ζ Pup.

The prior *XMM* detection of X-ray variability showed an overall decreasing trend with superimposed stochastic-seeming variability having an amplitude of approximately 20 per cent on days to months time-scale (Nazé et al. 2013). Interestingly, the X-ray output of the star seems more constant overall in the recent *Chandra* observations than it was about a decade earlier when the *XMM* observations were made. The *XMM* light curve implies that the changes to the wind properties of ζ Pup in the 18 yr interval between the two *Chandra* observing campaigns were neither smooth nor totally abrupt. Broad-band spectral trends in the *XMM* measurements also indicate that brighter X-ray emission is correlated with a hardening of the spectrum below 1.2 keV (Nazé et al. 2018), consistent with the trend we see in the wavelength-dependent line

Table 3. Emission line parameters.

Ion	Wavelength (Å)	τ_*	R_{o} (R_*)	Line flux (10^{-5} ph cm^{-2} s^{-1})
S XV	5.04, 5.07, 5.10	$0.12^{+.11}_{-.08}$	$1.48^{+.06}_{-.05}$	$3.28^{+.10}_{-.10}$
Si XIV	6.18	$0.55^{+.17}_{-.14}$	$1.34^{+.05}_{-.05}$	$1.06^{+.04}_{-.04}$
Si XIII	6.65, 6.69, 6.74	$0.66^{+.06}_{-.05}$	$1.60^{+.02}_{-.02}$	$15.4^{+.1}_{-.1}$
Mg XII	8.42	$1.01^{+.12}_{-.11}$	$1.54^{+.04}_{-.04}$	$3.95^{+.08}_{-.08}$
Mg XI	9.17, 9.23, 9.31	$0.80^{+.07}_{-.07}$	$1.77^{+.03}_{-.03}$	$23.5^{+.3}_{-.3}$
Ne X	10.24	$2.59^{+.19}_{-.16}$	$1.01^{+.41}_{-.01}$	$4.13^{+.15}_{-.14}$
Ne IX	11.54	$1.54^{+.29}_{-.25}$	$1.73^{+.10}_{-.11}$	$7.44^{+.25}_{-.24}$
Ne X	12.13	$3.10^{+.13}_{-.12}$	$1.01^{+.18}_{-.01}$	$30.1^{+.6}_{-.5}$
Fe XVII	15.01	$2.40^{+.34}_{-.30}$	$1.87^{+.14}_{-.16}$	$60.2^{+1.5}_{-1.5}$
Fe XVII	16.78	$3.87^{+.73}_{-.65}$	$1.46^{+.22}_{-.46}$	$32.4^{+1.7}_{-1.8}$
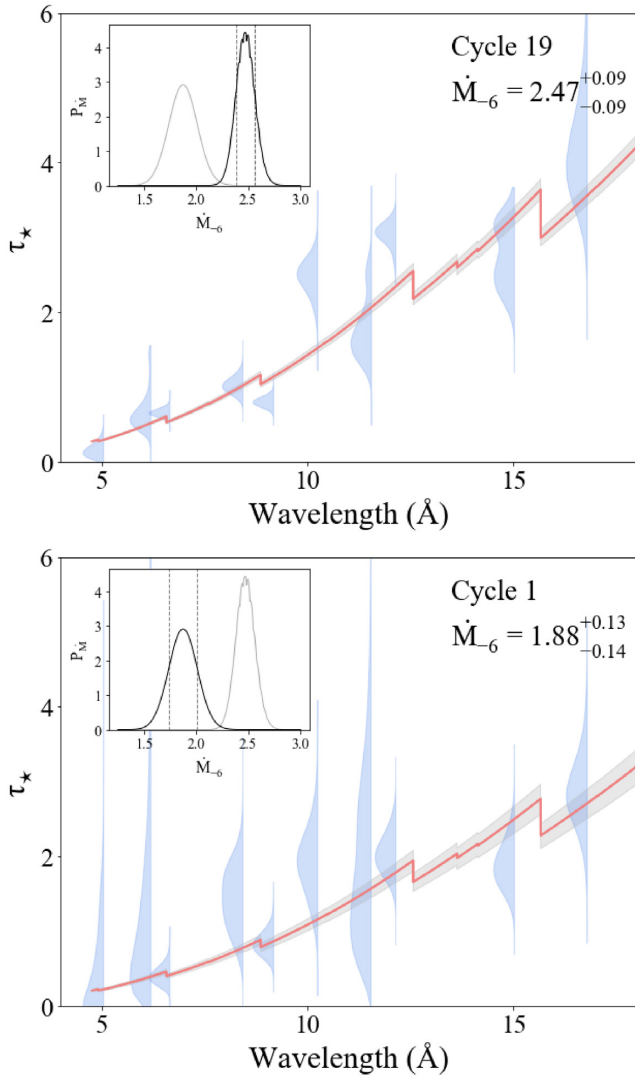
Figure 4. The τ_* probability distribution for each line is shown in light blue, while the best-fitting mass-loss rate model is shown in red, with the 68 per cent error band on the mass-loss rate shown in grey surrounding the best-fitting model. The cycle 19 results are shown in the top panel, while the reanalysed cycle 1 results are shown in the lower panel. The overall mass-loss rate probability distributions are shown in the insets, with the 68 per cent confidence limits shown graphically. The blue τ_* probability distributions are truncated at $\pm 5\sigma$.
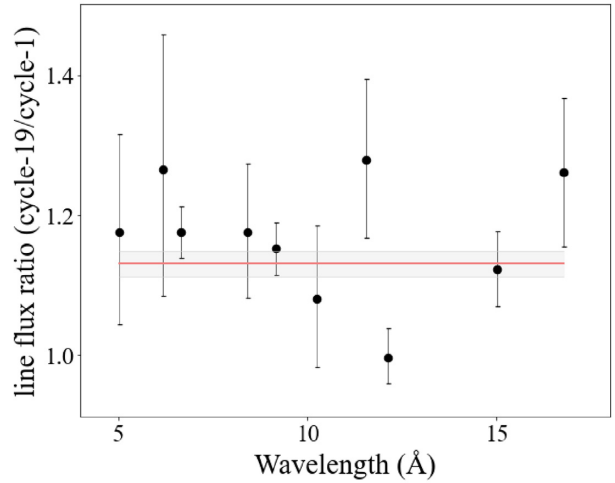

Figure 5. The line flux ratios with 68 per cent confidence limits for all the emission lines measured in both cycle 19 and cycle 1 show an average increase of 13 per cent from cycle 1 to cycle 19 (the red line). This increase has some modest wavelength dependence.

flux changes in the *Chandra* observations and with the expectations of increased wind column density leading to more soft X-ray attenuation.

5 CONCLUSIONS

The X-ray emission lines of ζ Pup show a systematic increase in blue shift and line shape between the two epochs of *Chandra* grating observations, separated by 18 yr. This change in the emission line profile morphology is consistent with increased X-ray absorption by the wind, indicative of a mass-loss rate increase of 40 per cent – a result that is significant at more than the 4σ level. The corresponding wavelength-dependent line flux increase is consistent with the intrinsic X-ray emission increasing along with the wind mass-loss rate, but the emergent line flux being affected by the increased wind absorption.

This result is quite surprising as ζ Pup is not known or expected to have a variable mass-loss rate beyond a few per cent associated with its observed stochastic and periodic low-level photometric variability. This certainly suggests that continued optical photometric monitoring and spectral monitoring would be recommended as well

perhaps as UV spectroscopy and a reanalysis of archival data. Other O and early B supergiants with wind signatures in their X-ray profiles could also be re-observed to see if they too change on years time-scales.

ACKNOWLEDGEMENTS

DATA AVAILABILITY

The X-ray spectral data underlying this article are available in the Chandra Data Archive at https://cxc.cfa.harvard.edu/cda/, and are uniquely identified with the observation identifiers (Obs IDs) listed in Table 1.

REFERENCES

Canizares C. R. et al., 2005, PASP, 117, 1144
Cash W., 1979, ApJ, 228, 939
Cassinelli J. P., Miller N. A., Waldron W. L., MacFarlane J. J., Cohen D. H., 2001, ApJ, 554, L55
Castor J. I., Abbott D. C., Klein R. I., 1975, ApJ, 195, 157
Cohen D. H., Leutenegger M. A., Grizzard K. T., Reed C. L., Kramer R. H., Owocki S. P., 2006, MNRAS, 368, 1905
Cohen D. H., Leutenegger M. A., Wollman E. E., Zsargó J., Hillier D. J., Townsend R. H. D., Owocki S. P., 2010, MNRAS, 405, 2391
Cohen D. H., Wollman E. E., Leutenegger M. A., Sundqvist J. O., Fullerton A. W., Zsargó J., Owocki S. P., 2014, MNRAS, 439, 908
David-Uraz A., Owocki S. P., Wade G. A., Sundqvist J. O., Kee N. D., 2017, MNRAS, 470, 3672
Foster A. R., Ji L., Smith R. K., Brickhouse N. S., 2012, ApJ, 756, 128
Howarth I. D., Prinja R. K., Massa D., 1995, ApJ, 452, L65
Huenemoerder D. P. et al., 2020, ApJ, 893, 52
Ignace R., 2001, ApJ, 549, L119
Kahn S. M., Leutenegger M. A., Cottam J., Rauw G., Vreux J. M., den Boggende A. J. F., Mewe R., Güdel M., 2001, A&A, 365, L312

Leutenegger M. A., Paerels F. B. S., Kahn S. M., Cohen D. H., 2006, ApJ, 650, 1096
MacFarlane J. J., Cassinelli J. P., Welsh B. Y., Vedder P. W., Vallerga J. V., Waldron W. L., 1991, ApJ, 380, 564
Massa D. et al., 1995, ApJ, 452, L53
Nazé Y., Oskinova L. M., Gosset E., 2013, ApJ, 763, 143
Nazé Y., Ramiaramanantsoa T., Stevens I. R., Howarth I. D., Moffat A. F. J., 2018, A&A, 609, A81
Nousek J. A., Shue D. R., 1989, ApJ, 342, 1207
Owocki S. P., Cohen D. H., 1999, ApJ, 520, 833
Owocki S. P., Cohen D. H., 2001, ApJ, 559, 1108
Owocki S. P., Sundqvist J. O., Cohen D. H., Gayley K. G., 2013, MNRAS, 429, 3379
Ramiaramanantsoa T. et al., 2018, MNRAS, 473, 5532
Sundqvist J. O., Owocki S. P., Puls J., 2018, A&A, 611, A17

APPENDIX A: CONTINUUM REGIONS

We carefully evaluated the wavelength regions used for fitting the continuum around each line, both by visually inspecting the data and by consulting the ATOMDB line list (Foster et al. 2012). Of course, a large number of very weak lines are distributed throughout the continuum, making it in reality a pseudo-continuum. The wavelength regions relatively free of contaminating lines are listed in Table A1. They and the associated continuum fits for the cycle 19 data are shown graphically in Fig. A1, along with the line fits themselves.

Table A1. Emission line pseudo-continuum regions.

| Ion	Line wavelength (Å)	Continuum ranges (Å)
S XV	5.04, 5.07, 5.10	4.60–4.70, 4.76–4.95, 5.25–5.38, 5.43–5.60
Si XIV	6.18	6.05–6.09, 6.23–6.26, 6.33–6.40
Si XIII	6.65, 6.69, 6.74	6.30–6.50, 6.83–7.00
Mg XII	8.42	8.15–8.32, 8.64–8.80
Mg XI	9.17, 9.23, 9.31	8.60–8.80, 8.83–8.93, 9.00–9.04, 9.50–9.61
Ne X	10.24	9.73–9.93, 10.12–10.15, 10.345–10.39
Ne IX	11.54	11.32–11.39, 11.65–11.83
Ne X	12.13	11.94–12.03, 12.315–12.345
Fe XVII	15.01	14.63–14.90
Fe XVII	16.78	16.45–16.60, 16.89–16.90
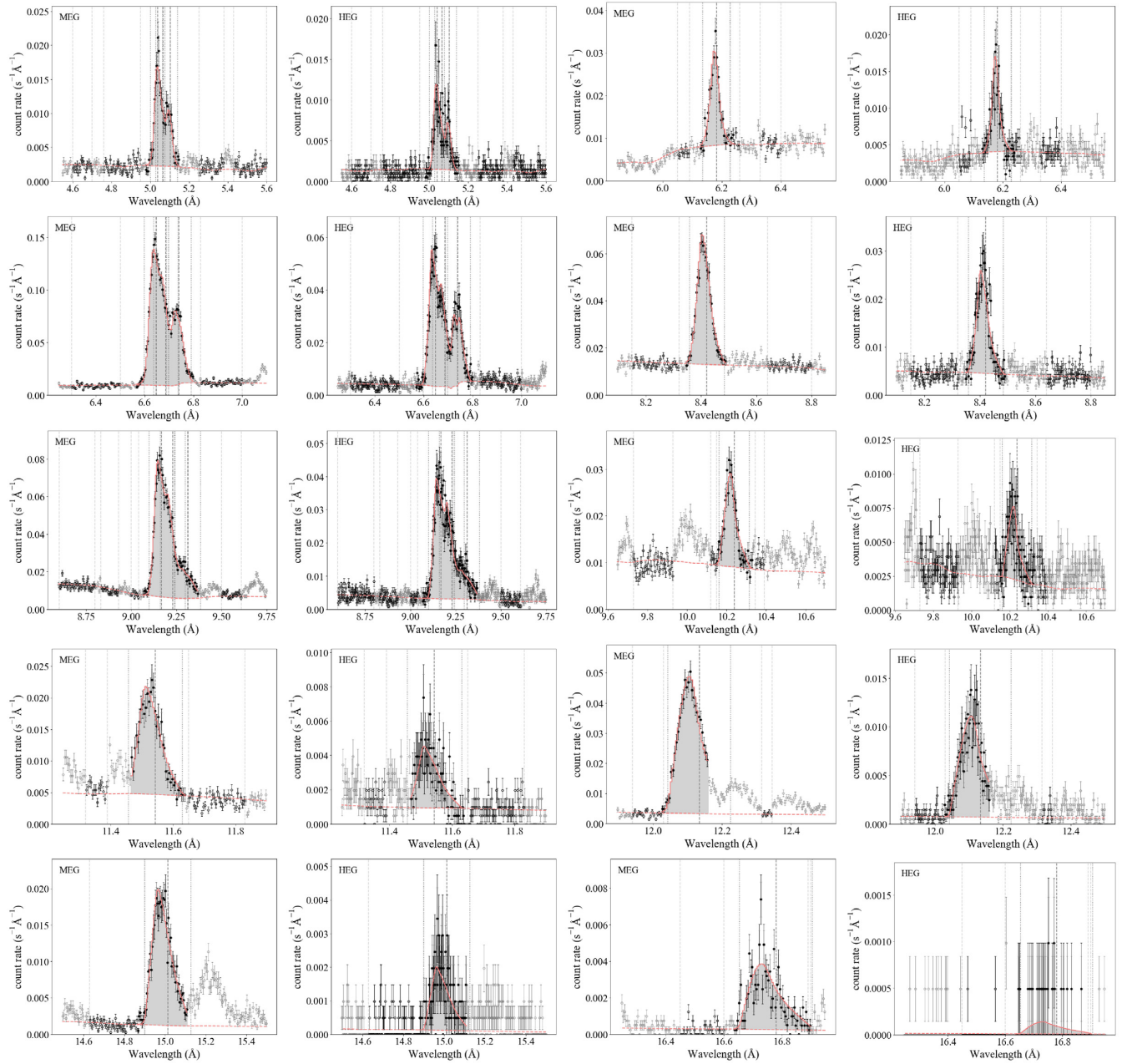
Figure A1. Combined 21 cycle 19 Obs IDs are shown for each of the 10 lines in MEG and HEG pairs. The pseudo-continuum around each line is indicated, with both vertical dotted lines and darkened data points showing the regions that were used for the fitting.

APPENDIX B: WIND PROFILE FITTING OF INDIVIDUAL LINES

The fits to each line and line complex are shown in Fig. B1 for the cycle 19 data and in Fig. B2 for the cycle 1 data.
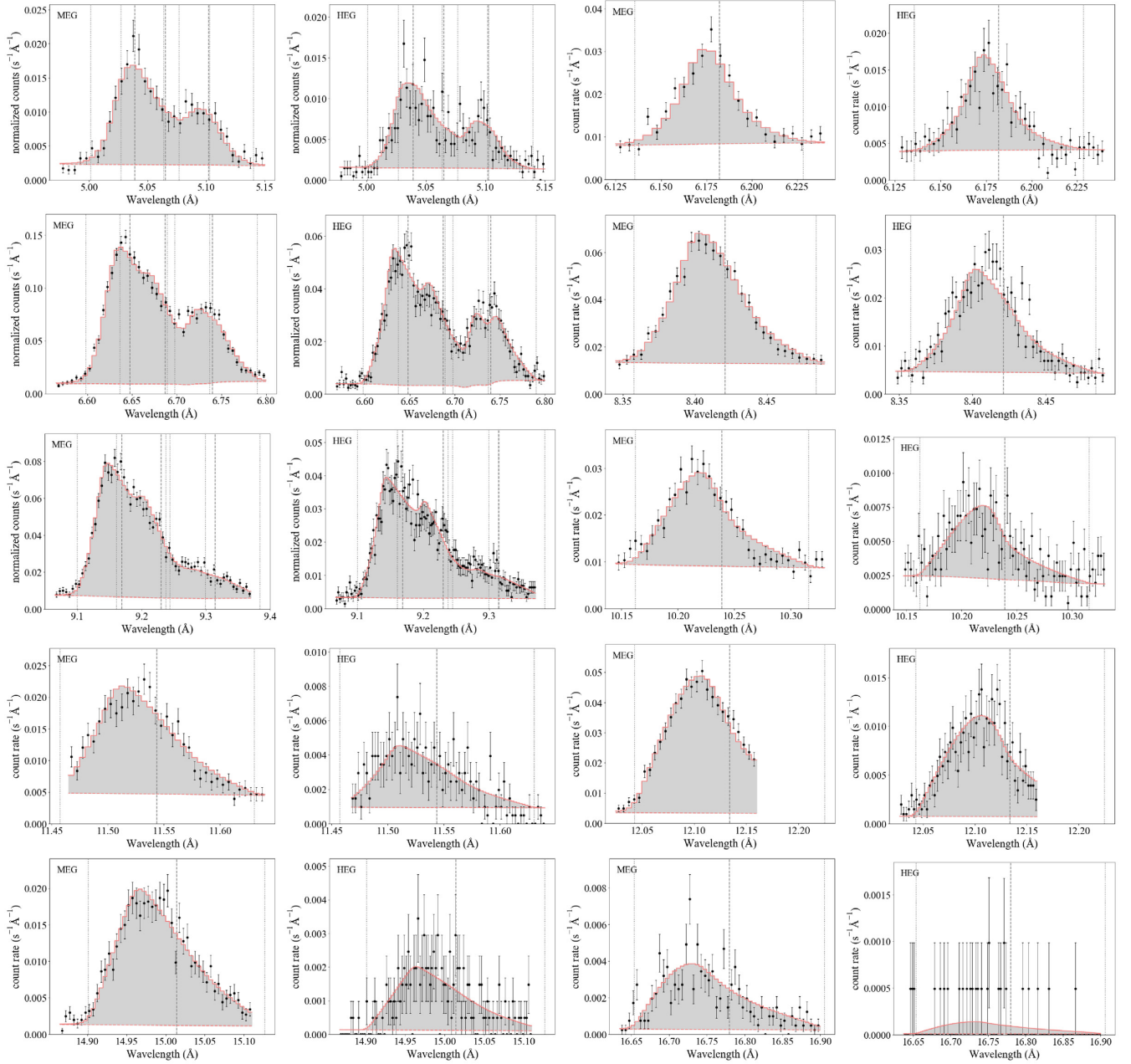
Figure B1. We show wind profile models (on top of continuum models) fit to the cycle 19 data for each of the 10 lines and line complexes analysed in this paper. For each line or complex, we show a pair of panels: combined first order MEG (left; so first and third columns) and HEG (right; so second and fourth columns). A darker vertical dashed line indicates the rest wavelength of each line, while lighter flanking vertical lines indicate the Doppler shifted wavelengths associated with the wind terminal velocity of 2250 km s^{-1}.
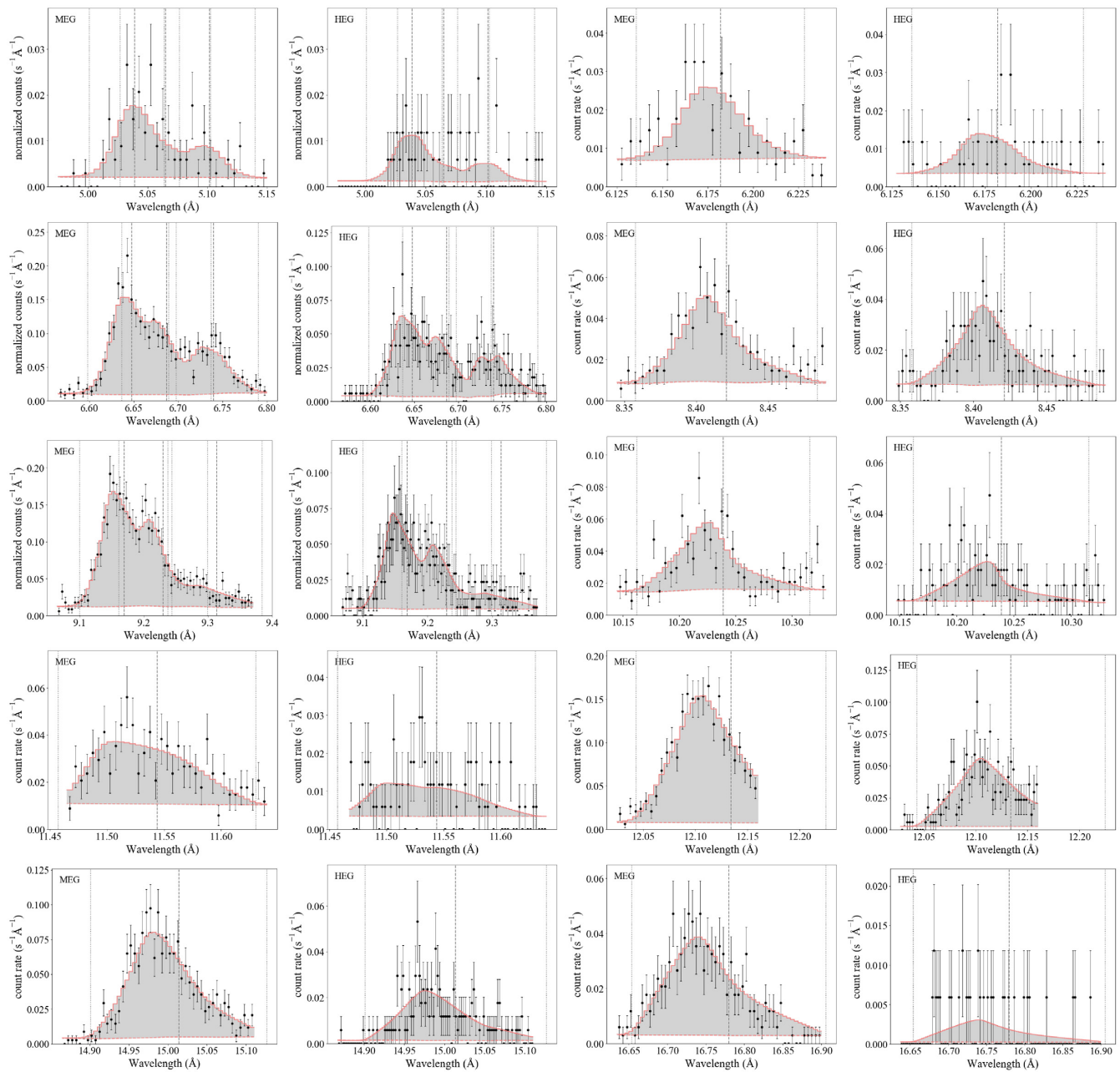
Figure B2. Same as Fig. B1 but for cycle 1.

This paper has been typeset from a TEX/LATEX file prepared by the author.